Full Length Research Paper

Simulation of sea surface current velocity from synthetic aperture radar (SAR) data

Maged Marghany* and Mazlan Hashim

Institute of Geospatial Science and Technology (INSTEG), UniversitiTeknologi Malaysia 81310 UTM, Skudai, JohoreBahru, Malaysia.

This study is done to solve the Doppler spectra equation by involving two -dimensional Fourier transform (2DFFT) to obtain a linear formula of sea radial component. The problem of influence of bandwidth on imaging moving ocean surface is analytically solved. Based on the maximum peak of Doppler spectra, the horizontal surface current is computed. The Doppler spectra model has been performed in the RADARSAT-1 SAR data. This study concludes that Doppler spectra model is an appropriate method to compute the sea surface current in the RADARSAT-1 SAR data.

Key words: RADARSAT-1 SAR, sea surface current, two-dimensional Fourier transform (2DFFT), Doppler spectra.

INTRODUCTION

Complexity of ocean nature needs standard instruments and procedures to comprehend. Despite advanced technology of ocean *in situ* measurements, large ocean area cannot be surveyed effortlessly. In reality, weather circumstances induce storms, which cause disasters in coastal zone that do not allow oceanographers and researchers to acquire timeless and effortless in situ measurements. Recently, researchers have shown an increased interest in ocean studies using remote sensing technology, which can image large-scale ocean area and provide precise information on air-sea surface interactions (Wittgenstein, 1992). Besides, ocean surface features such as fronts, oil spills, and look-likes, and eddy mesoscale can be detected using remote sensing technology. With remote sensing instruments available, the microwave imaging radar is the only system with an all-weather potential to acquire measurements of air-sea interaction.

It is well known that synthetic aperture radar (SAR) can image ocean surface current gradient. However, the imaging mechanisms are complicated since the sea surface motion variations are imaged through energy transfer toward the waves. According to Inglanda and

Garello (2002), the energy transfer between the current gradients and the waves is described by the action balance equation (ABE) which gives the nonlinear relationship between the surface current and the perturbation of the wave spectrum from its equilibrium. Several studies have been conducted to solve the action balance equation by using the numerical methods to compute the normalized radar cross section (NRCS) of sea surface roughness, and then utilizing the modulation model to retrieve the surface current. Nevertheless, the linearization of ABE allows the production of weak linear hydrodynamic modulation, which involves the problem of the relaxation rate or wave growth. Furthermore, Inglanda and Garello (1999) have used Volterra series expansion to express the non-linear relationship between the surface current and the SAR image pixel intensity. With Volterra model, they can compute the energy contained in the different orders (linear, quadratic and higher) and by using inverse of Volterra model, the sea surface current can be estimated. In this paper, we address the question of the impact of tidal force in inducing ocean current movement. According to Wrytki (1961), Zelin at el. (2000) and Maged and Mazlan (2006), the South China Sea is characterized by peak tidal currents commonly in excess of 1.6 m/s (Maged and Mazlan, 2009). This indicates that ABE model cannot be used to extract sea surface current movement in the South China

---

*Corresponding author. E-mail: magedupm@hotmail.com.

Sea. Two hypotheses examined are: (i) Doppler spectra model that can compute the sea surface gradient variation, and (ii) horizontal sea surface current that can be retrieved from Doppler spectra variation by computing radial component of SAR ocean current to real ocean current. The main objective of this study is to solve the Doppler phase equation to obtain the sea surface current by using SAR data.

RESEARCH METHODS

Study area

The study area is located in the east coast of Kuala Terengganu which is located on the eastern part of the Peninsula of Malaysia. This area is located between the longitudes 102°50'00"N to 103°40'00"N and latitudes 5°25'00"E to 5°40'00"E (Figure 1). According to Maged et al. (2010) the coastal water less than 50 nautical miles from shore is quite shallow with the deepest area being approximately 50 m.

The bottom has gentle slopes, gradually deepening towards the open sea. A clear feature of this area is the primary hydrologic communications between the estuary and the South China Sea which is the largest estuary along the Kuala Terengganu (Maged et al., 2009). East coast of peninsular Malaysia borders the South China Sea, the largest water body in Southeast Asia and faces the continental shelf of Sunda platform, which has water depths not exceeding 100 m. Air temperature is uniform throughout the year, varying from 24 to 28°C with an average humidity of approximately 80%. The average amount of cloud covering over the sea 50 to75% is also constant (Zelina et al., 2000). The Northeast and Southeast trade winds converge is near the Equator. The convergence of these winds causes air mass to rise and condense at high altitude. This narrow area of convergence is called Inter-Topical Convergence Zone (ITCZ). The ITCZ passes Peninsular Malaysia twice a year (Zelina et al., 2000). The climate dominated by the ITCZ, which moves through the area in a seasonal cycle brings the Northeast monsoon between November and March and the Southwest monsoon between May and September. Annual rainfall is greater than 300 mm on the coast and 250 on the islands (Zelina et al., 2000).

According to Maged et al. (2009) there are four seasons: the two monsoons and the two transitional inter-monsoon periods. The monsoon winds and tidal effects (Maged et al., 2010) affect the seas around Malaysia. The winds during the Northeast monsoon are normally stronger than the Southwest monsoon (Wrytki, 1961; Zelina et al., 2000). The accompanying waves are with a height that exceeds 3 m (Chua, 1984).

Data collection

The latest technologies have the advantage of allowing many observations to be carried out simultaneously such as sea surface current patterns form SAR imagery and Acoustic Wave and Current (AWAC) equipment. Data used in the study are divided into three groups: remotely sensed, in situ measurements, and ancillary data. Sequences of different RADARSAT-1 SAR images were acquired over the study area on March 21, 25, and 31, 2005, respectively. The RADARSAT-1 SAR images were acquired in different incidence angles and modes (Table 1).

MODEL

SAR utilizes the Doppler shift of the complex received field to locate

scatterers in the flight direction. This complex field and its associated residual Doppler shift can be used to infer the velocity of these scatterers as adverted by ocean currents (Hasselman, 1980; Rufenach et al., 1983). The analysis method to extract ocean currents by using the Doppler spectral shift is given in details. The analysis method is useful in inferring ocean currents from the RADARSAT-1 SAR Wide-3, High Extended-6, and Standard-2 modes (Figure 2).

Following Rufenach et al. (1983), the concept of RADARSAT-1 SAR geometry for sea surface current retrieval is shown in Figure 3. The spectral density is a response from infinitesimal point scatterers. A closed form solution can be given for the Doppler spectral density as the following expression (Gonzalez et al., 1980 and Rufenach et al., 1983):

$$G(x_0, \omega) = H(\omega)e^{i\omega x_0/V} \int_{-\infty}^{\infty} \exp\left[-\frac{2}{T_s^2}\left(1 + \left(\frac{T_s}{T}\right)^2 - \frac{ibT_s^2}{4}\right)\tau^2 \right.$$
$$\left. -\frac{4}{T_s}\left(\frac{x_0}{VT_s} + i\frac{\omega' T_s}{4}\right)\tau - \frac{2x_0^2}{V^2 T_s^2} \right] d\tau \tag{1}$$

Where $x_0 = vt$ is the location of a point target in the SAR image, T_s is the Gaussian function with width, V is the satellite velocity = 6212m/s, τ is the delay time = $t - x_0/V$ and b is the chirp rate = $2kv^2/R$. Equation (1) has been solved to determine the spectral magnitude. Image intensity related to spectral magnitude is used to find out the radial current velocity. Equation (1) is equivalent to the following equation (2):

$$G(x_0, \omega) = H(\omega)e^{i\omega x_0/V} \int_{-\infty}^{\infty} \exp\left[-\frac{2}{T_s^2}\left(1 + \left(\frac{T_s}{T}\right)^2 - \frac{ibT_s^2}{4}\right)\tau^2 \right.$$
$$\left. -\frac{4}{T_s}\left(\frac{x_0}{VT_s} + i\frac{\omega' T_s}{4}\right)\tau \right] \times \exp\left[-\frac{2x_0^2}{V^2 T_s^2} \right] d\tau \tag{2}$$

Simplifying equation (2) we obtain

$$G(x_0, \omega) = H(\omega)\exp\left[\frac{i\omega x_0}{V} - \frac{2x_0^2}{V^2 T_s^2} \right] \int_{-\infty}^{\infty} \exp\left[-\frac{2}{T_s^2}\left(1 + \left(\frac{T_s}{T}\right)^2 - \frac{ibT_s^2}{4}\right)\tau^2 \right.$$
$$\left. -\frac{4}{T_s}\left(\frac{x_0}{VT_s} + i\frac{\omega' T_s}{4}\right)\tau \right] d\tau \tag{3}$$

By calculating the integral in the right side of equation (3) yields

$$G(x_0, \omega) = H(\omega)\exp\left[\frac{i\omega x_0}{V} - \frac{2x_0^2}{V^2 T_s^2} \right] \cdot \frac{\sqrt{\pi}}{\sqrt{\frac{2}{T_s^2}\left(1 + \left(\frac{T_s}{T}\right)^2 - \frac{ibT_s^2}{4}\right)}}$$
$$\cdot \exp\left[\frac{\left(\frac{4}{T_s}\left(\frac{x_0}{VT_s} + i\frac{\omega' T_s}{4}\right)\right)^2}{\frac{8}{T_s^2}\left(1 + \left(\frac{T_s}{T}\right)^2 - \frac{ibT_s^2}{4}\right)} \right] \tag{4}$$
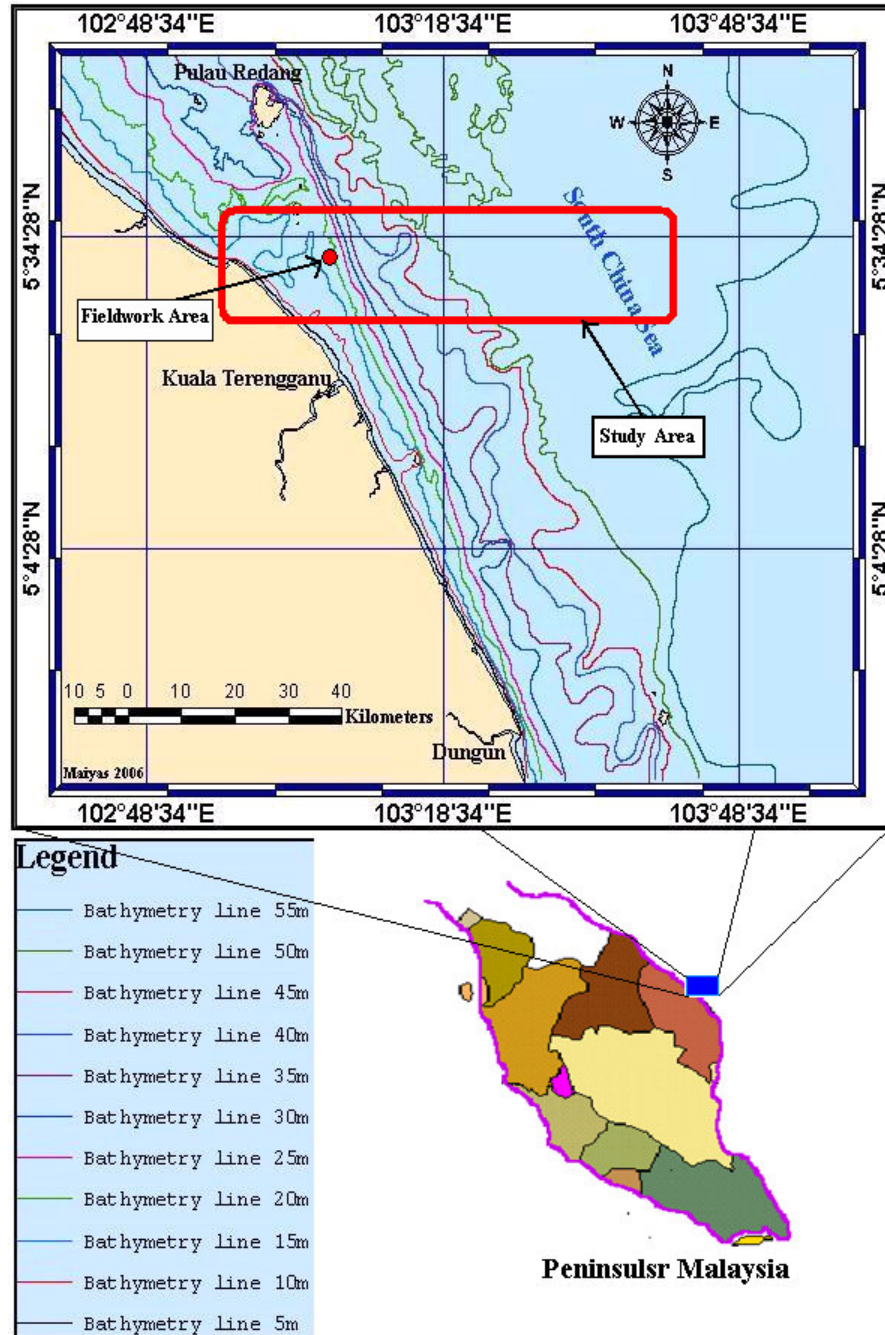
Figure 1. Location of study area.

Table 1. RADARSAT-1 SAR image description.

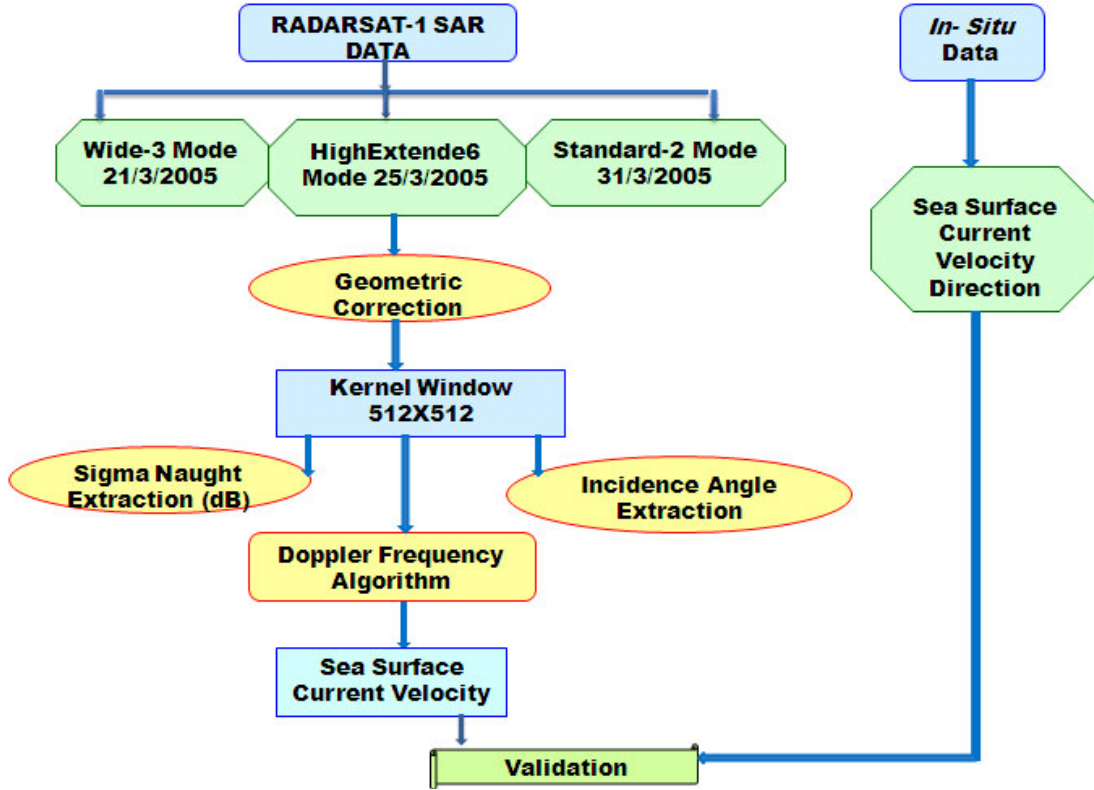| Start time	Orbit	Beam	Incidence Angle (deg)	Coverage (Km²)
03/20/2005 6:48:57 AM	150D	Wide-3 (Descending)	38-45	10513
03/25/2005 7:39:49 AM	201A	Extended High-6 (Ascending)	56-59	3929
03/30/2005 6:57:16 AM	293D	Standard-2 (Descending)	24-31	7694

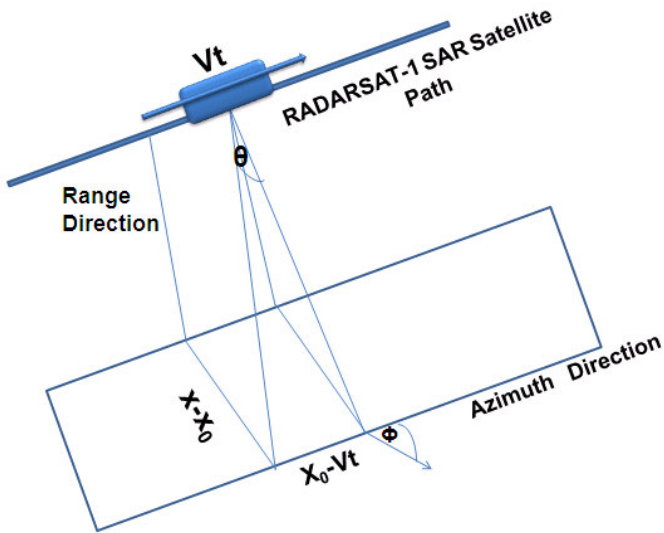**Figure 2.** Block diagram for sea surface current retrieval from RADARSAT-1 SAR different mode data.

Figure 3. Geometry concept for retrieval sea surface current from RADARSAT-1 SAR.

Simplifying equation (4) we get

$$G(x_0,\omega)=H(\omega)\exp\left[\frac{i\omega x_0}{V}-\frac{2x_0^2}{VT_s^2}\right]\left(\frac{\sqrt{\pi}}{\sqrt{2}}\right)\frac{T_s}{\left[1+(T_s/T)^2-i(bT_s^2/4)\right]^{1/2}}$$

$$.\exp\left[\frac{\dfrac{16}{T_s^2}\left[\left(\dfrac{x_0}{VT_s}\right)^2+2\left(\dfrac{x_0}{VT_s}\right)\left(\dfrac{i\omega'T_s}{4}\right)-\dfrac{\omega'^2 T_s^2}{16}\right]}{\dfrac{8}{T_s^2}\left[1+(T_s/T)^2-i(bT_s^2/4)\right]}\right] \tag{5}$$

It follows that

$$G(x_0,\omega)=H(\omega)\exp\left[\frac{i\omega x_0}{V}-\frac{2x_0^2}{VT_s^2}\right]\left(\frac{\pi}{2}\right)^{1/2}\cdot\frac{T_s}{\left[1+(T_s/T)^2-i(bT_s^2/4)\right]}$$

$$.\exp\left[\frac{2(x_0/VT_s)^2+i(x_0/V)\omega-(\omega^2 T_s/8)}{1+(T_s/T)^2-i(bT_s^2/4)}\right] \tag{6}$$

Hence,

$$G(x_0,\omega)=H(\omega)\exp\left[\frac{i\omega x_0}{V}-\frac{2x_0^2}{V^2T_s^2}\right]\left(\frac{\pi}{2}\right)^{1/2}\cdot\frac{T_s}{\left[1+(T_s/T)^2-i(bT_s^2/4)\right]}$$

$$.\exp\left[\frac{2(x_0/VT_s)^2-(\omega'^2 T_s^2/8)+i(x_0/V)\omega'}{1+(T_s/T)^2-i(bT_s^2/4)}\right] \tag{7}$$

Approximating the square of equation (7) we obtain The Doppler

spectral density which is

$$\left|G(x_0,\omega)\right|^2 \cong \frac{4\pi^2}{b^2}\exp\left[-\left(\frac{2}{bT_h}\right)^2\omega^2\right]$$

$$\exp\left[-\left(\frac{2}{bT}\right)^2(\omega-\omega_d)^2\right]\exp\left[-\left(\frac{2}{bT}\right)^2\left(\omega-\omega_d-\frac{bx_0}{V}\right)^2\right]$$

(8)

Where the approximation $\left(bT^2/4\right)$, $\left(bT_h^2/4\right)$, and $\left(bT_s^2/4\right) > 1$ have been assumed to simplify this expression. This assumption, large time-bandwidth products, is reasonable for most radar and processor characteristics. The position of the Doppler spectral density peak, $\omega_{\max}$, occurs where the argument of (8) is maximum

$$\omega_{\max} = \frac{\omega_d\left(1+(T_s/T)^2\right)+b(x_0/V)}{1+(T_s/T)^2+(T_s/T_h)^2}$$

(9)

Or in the terms of system bandwidths (Hasselmann et al., 1980),

$$\omega_{\max} = \frac{\omega_d\left(1+(\Delta\omega_s/\Delta\omega_a)^2\right)+b(x_0/V)}{1+(\Delta\omega_s/\Delta\omega_a)^2+(\Delta\omega_s/\Delta\omega_h)^2}$$

(10)

Where the $\Delta\omega_a$ is the received signal azimuthal bandwidth $=bT$, $\Delta\omega_h$ is the processor bandwidth $=bT_h$, and $\Delta\omega_s$ is the laser weighting bandwidth. Equations (8), (9), and (10) give the Doppler spectral density dependence for a point target located at x_0. The processor bandwidth $\Delta\omega_h$ is much larger than the laser weighting bandwidth $\Delta\omega_s$, the received signal bandwidth $\Delta\omega_h$ and the received signal bandwidth $\Delta\omega_a$. Then (10) reduces to (Hasselmann et al., 1980):

$$\omega_{\max} = \omega_d + b\left(\frac{x_0}{V}\right)\left(1+\left(\frac{\Delta\omega_s}{\Delta\omega_a}\right)^2\right)^{-1}$$

(11)

Therefore, under the above assumptions, the point target response of the Doppler spectral density peak is located at a position determined by the radial component of point target velocity. This result, (11), is the classic Doppler expression in terms of temporal frequency (Shuchman et al., 1979; Gonzalez et al., 1980).

For radar signals scattered from the ocean surface, a distributed surface must be considered rather than a point target. The scattering surface may usually be considered statistically white for typical SAR resolution cell sizes. In other words, the scattering surface implies uniformly distributed phases (Rufenach and Alpers, 1981; Hasselmann, 1980). Therefore, the phases of the complex field at the frequency plane are uncorrelated such that

$$\langle dl(x_0)dl^*(x_0')\rangle = \sigma(x_0)\delta(x_0-x_0')dx_0'$$

(12)

Where $\sigma(x_0)$ represents the radar scattering cross section per unit surface area and the angular brackets denote averaging over sub-resolution point targets or equivalently infinitesimal scattering

elements. The complex field at the frequency plane for a distributed surface is given by summing the spatial contributions from the individual infinitesimal scatterers,

$$G(\omega) = \int_{-\infty}^{\infty} G(x_0,\omega)dl(x_0)$$

(13)

Equation (13) is used for a distributed surface such as land or ocean which can be represented as a random ensemble of scatterers. Therefore, the average Doppler spectral intensity is obtained after forming the square modulus,

$$I(\omega) = \langle\left|G(\omega)^2\right|\rangle = \int_{-\infty}^{\infty}\sigma(x_0)\left|G(x_0,\omega)\right|^2 dx_0$$

(14)

Equation (14) illustrates several important points that influence ocean current measurements. The radar cross section may vary with x_0 because of several factors such as gradients in surface winds and tilt and hydrodynamical effects of the ocean waves (Alpers et al., 1981). Under certain conditions we may approximate $\sigma(x_0) \cong \sigma$, a constant; such a condition may exist for low wave heights, say in protected coastal regions. The Doppler spectral intensity can be given in closed form by assuming uniform radar cross section

$$I(\omega) = \frac{2\sigma\pi^{5/2}VT_s}{b^2}\exp\left[-\left(\frac{2}{bt_h}\right)^2\omega^2\right]\exp\left[-\left(\frac{2}{bT}\right)^2(\omega-\omega_d)^2\right]$$

. (15)

Equation (15) illustrates that the Doppler spectrum for a uniform distributed scene is independent of T_s the laser weighting. Whereas for a point target or a non-uniform distributed scene the laser weighting influences the spectral density position. Following the procedure used to obtain the Doppler spectral density peak, the Doppler spectral intensity peak has been obtained based on (15),

$$\omega_{\max} = \omega_d\left(1+\left(\frac{T}{T_h}\right)^2\right)^{-1} = \omega_d\left(1+\left(\frac{\Delta\omega_a}{\Delta\omega_h}\right)^2\right)^{-1}$$

. (16)

First, if the processor bandwidth is much larger than signal bandwidth $\Delta\omega_h\Delta\omega_a$. If $\Delta\omega_h = \Delta\omega_a$ then $\omega_{\max} = \omega_d/2$, which implies Doppler shifts value. If the ratio relating these bandwidths is $\Delta\omega_a = \alpha\Delta\omega_h$, where $0 < \alpha \le 1.0$, then $\omega_{\max} = \omega_d/(1+\alpha^2)$, implying that $\omega_d < \omega_{\max} \le \omega_d/2$. The special optical processing of the received signal to obtain the Doppler spectral intensity consists of a transforming lens located at the images plane. The spectral intensity is then observed at a specified distance behind the image plane. A photomultiplier detects the intensity at the frequency plane by scanning the azimuth spectral profiles.

The estimate of Doppler frequency in (16) is obtained from the difference between the peak frequencies for a scan corresponding to land near Porlier Pass and Porlier Pass Ocean scan which includes the radial component of the horizontal ocean current. Errors in the location of the Doppler peak due to azimuthal antenna pointing should be minimized since the differencing occurs nearly simultaneously. Spatial filter is placed at the image plane such that only the area of interest is selected. A spatial filter 512 X 512 pixels was selected. The image intensity using equations (1) to (16) and following Rufenach and Alpers (1981) is

$$I(x) = \frac{\pi}{2}T^2 \int_{\infty}^{\infty} \sigma(x_0) \frac{\rho_a}{\rho_a'} \exp\left[-\frac{\pi^2}{\rho_a'^2}\left(x - x_0 - \frac{R}{V}u_r\right)^2\right]$$

(17)

Where

$$\rho_a' = N' \rho_a \left[1 + \frac{1}{N'^2}\left(\frac{\pi T^2}{\lambda}a_r\right)^2\right]^{1/2}$$

(18)

ρ_a is the stationary target resolution, and

$$N' = \left[1 + \left(\frac{\Delta\omega_a}{\Delta\omega_s}\right)^2 + \left(\frac{\Delta\omega_a}{\Delta\omega_h}\right)^2\right]^{1/2}$$

(19)

The azimuthal resolution ρ_a' based on (18) is

$$\rho_a' = 1.12\rho_a\left[1 + 0.8\left(\frac{\pi T^2}{\lambda}a_r\right)^2\right]^{1/2}$$

(20)

Which is the degraded resolution caused by orbital acceleration a_2 and can be compared to the previous result based on an infinite processor bandwidth, $\Delta\omega_h > \Delta\omega_a$, implying $N' =1$. The study area was selected for measurements and the geometry was determined to minimize the effects of the long gravity waves and maximize the magnitude of the ocean currents. The RADARSAT-1 SAR ocean current values have been converted to the horizontal ocean current V_c on the ocean surface. The radial component of ocean current deduced from RADARSAT-1 SAR images is given in terms of the Doppler peak frequency shift, f_{max}, based on (18); therefore, the horizontal ocean current is

$$V_c = \frac{2}{N}\left[\frac{\lambda V\left(1 + \Delta f_a / \Delta f_h\right)^2}{2\rho_a \sin\theta \sin\Phi}\right]\left(\Delta f_a\right)^{-1}$$

(21)

$\Delta f_a = \left(\Delta\omega_a / 2\pi\right)$ and $\Delta f_h = \left(\Delta\omega_h / 2\pi\right)$ have been used to compute the frequency. The received signal bandwidth of RADARSAT-1 C-band for the Standard 2 has been used in to retrieve sea surface current.

RESULTS AND DISCUSSION

The sea surface current velocities are simulated and modelled from RADARSAT-1 SAR different mode data of Wide-3, Extended High-6, and Standard-2 modes, respectively. The simulation has been done along the range direction. The simulated velocity is taken across the location of AWAC rider bouy (Figure 4). The test area is shown in Figure 1 which is extended from inshore to
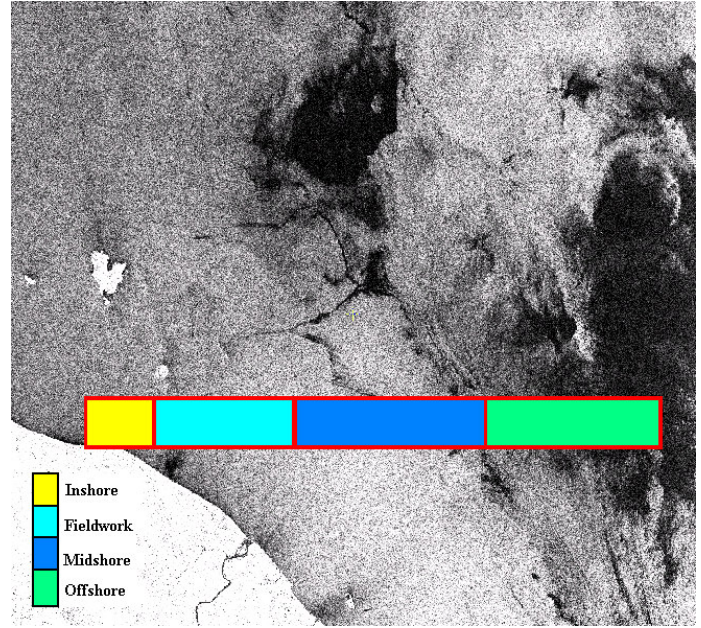

Figure 4. Selected test area.

offshore and approximately covered 100 km along the coastal water of Kuala Terengganu, Malaysia.

Figures 5 to 7 show the sea surface current velocity variations along the range direction as function of radar cross section, Doppler frequency, incident angle and ocean bathymetry for theWide-3(W3) mode, Standard-2 (S2) and the Extended High-6 mode data, respectively. The backscatter intensities are assorted between -17 dB and -22 dB in W3, -21 and -23dB in Extended High-6, and -13dB to -22dB in S2 mode data, respectively. The Doppler frequency spectra are ranged between 10 to 50 Hz in W3, 0-70 Hz in Extended High-6, and 10-700 Hz in S2 mode data. The incidence angles are varied between 38.5° to 44° in W3, 56.6° to 57.4° in Extended High-6, and 25.5° to 30.5° in S2 mode data, respectively. Under these circumstances, the current velocity spatial variations are a function of Doppler frequency spectra and incidence angle. W3 mode data capture maximum current velocity of 0.27 m s-1 in the onshore with highest Doppler frequency of 33 Hz, and incidence angle of 41°. The velocity varies gradually in midshore and offshore with 0.25 and 0.24 m s^{-1}, respectively. The midshore and offshore current velocities simulated from Doppler frequency spectra of 27 and 19 Hz, respectively. However, the incidence angle increases from 41° to be 45° with gradual decreasing of spatial variation of current velocity and Doppler frequency spectra (Figure 5).

In Extended High-6 mode, the sea surface current velocity is ranged between 0.30 to 0.35 ms^{-1} with extreme Doppler frequency spectra of 70 Hz and incidence angle of 59.6° (Figure 6). In contrast to W3 and Extended High-6 mode, S2 shows lowest offshore backscatter of -22dB opposed to highest Doppler frequency spectra of 800
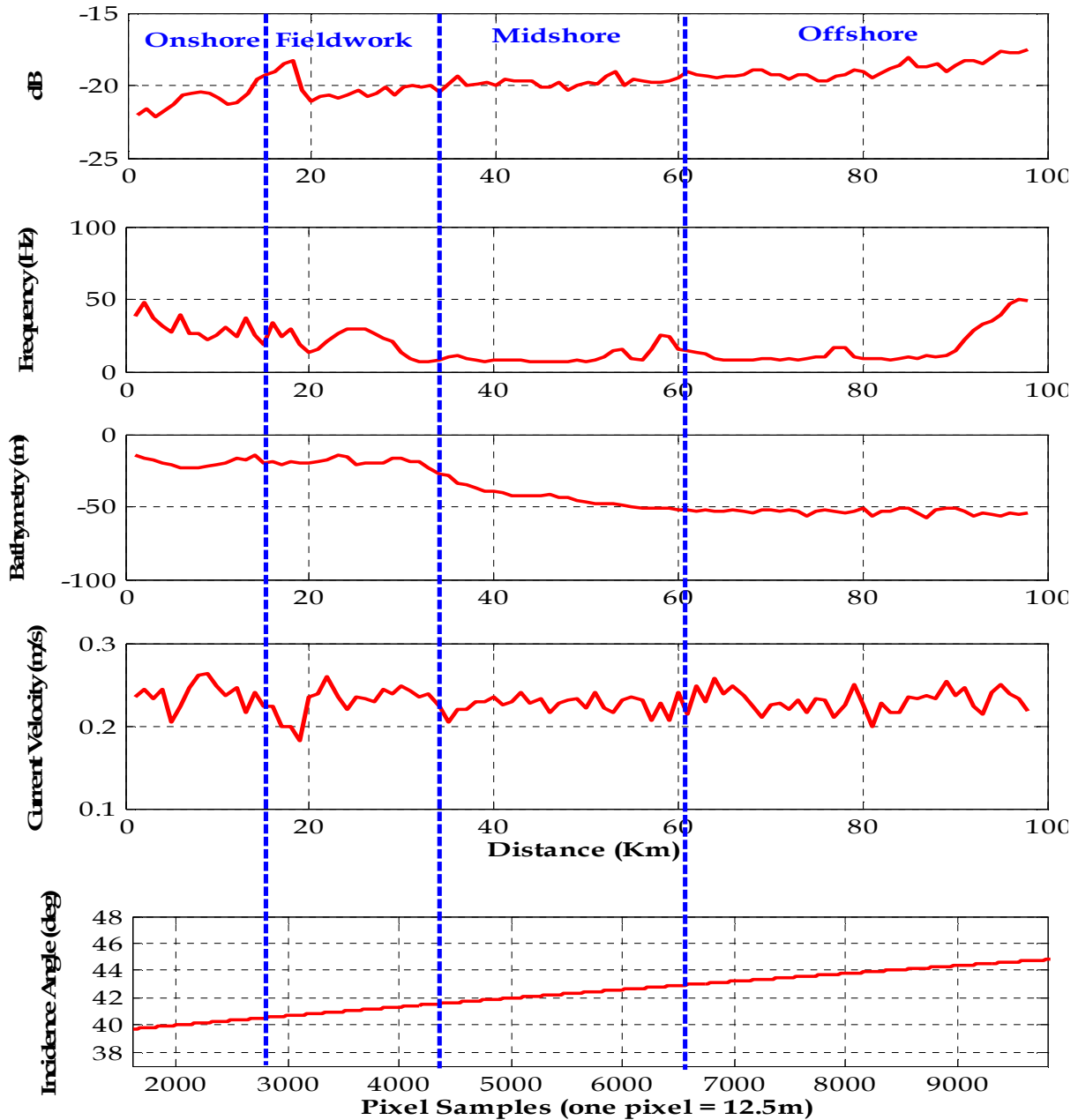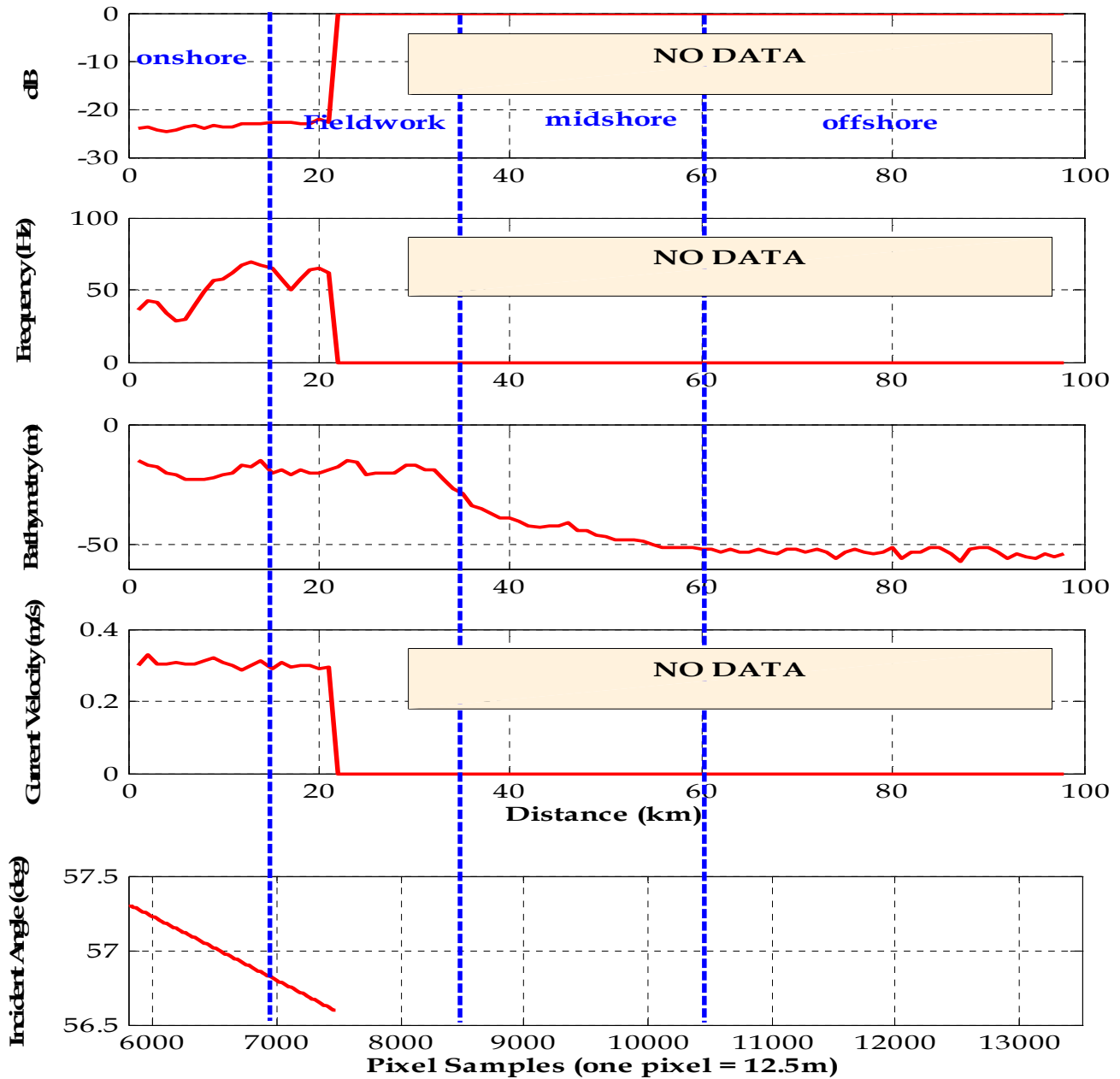
Figure 5. Comparison between physical properties of RADARSAT-1 SAR wide-3 mode and the Bathymetry along the study area.

Hz, inciedence angle of 30° and sea surface current of 0.5 m s-1, respectively (Figure 7). In addition, the midshore sea surface has steady pattern which varied between 0.65 to 0.75 ms^{-1}. As a result, the backscatter intensity, the Doppler frequency spectra and incidence angles have steady physical characteristics. The backscatter intensity varies between -11 to -13 dB, the Doppler frequency spectra change gradually from 50-100 Hz, and incidence angle alters slightly from 27.8° to 28.3°. In comparison to midshore and offshore sea surface currents, the onshore sea surface current is dominated with maximum current velocity of 0.75 ms^{-1} with shallower incidence angle that varied between 25° to 26° and Doppler frequency spectra of 200 Hz.

Table 1 shows an average sea surface current retrieval from W3, Extended High-6, and S3 mode data. It is interesting to find the offshore sea surface current increased towards onshore. According to Maged et al. (2009), the decreasing of onshore bathymetry speeds up the current velocity due to friction and creates a high backscatter intensity signature in SAR data followed by increasing of Doppler frequency shift. These results
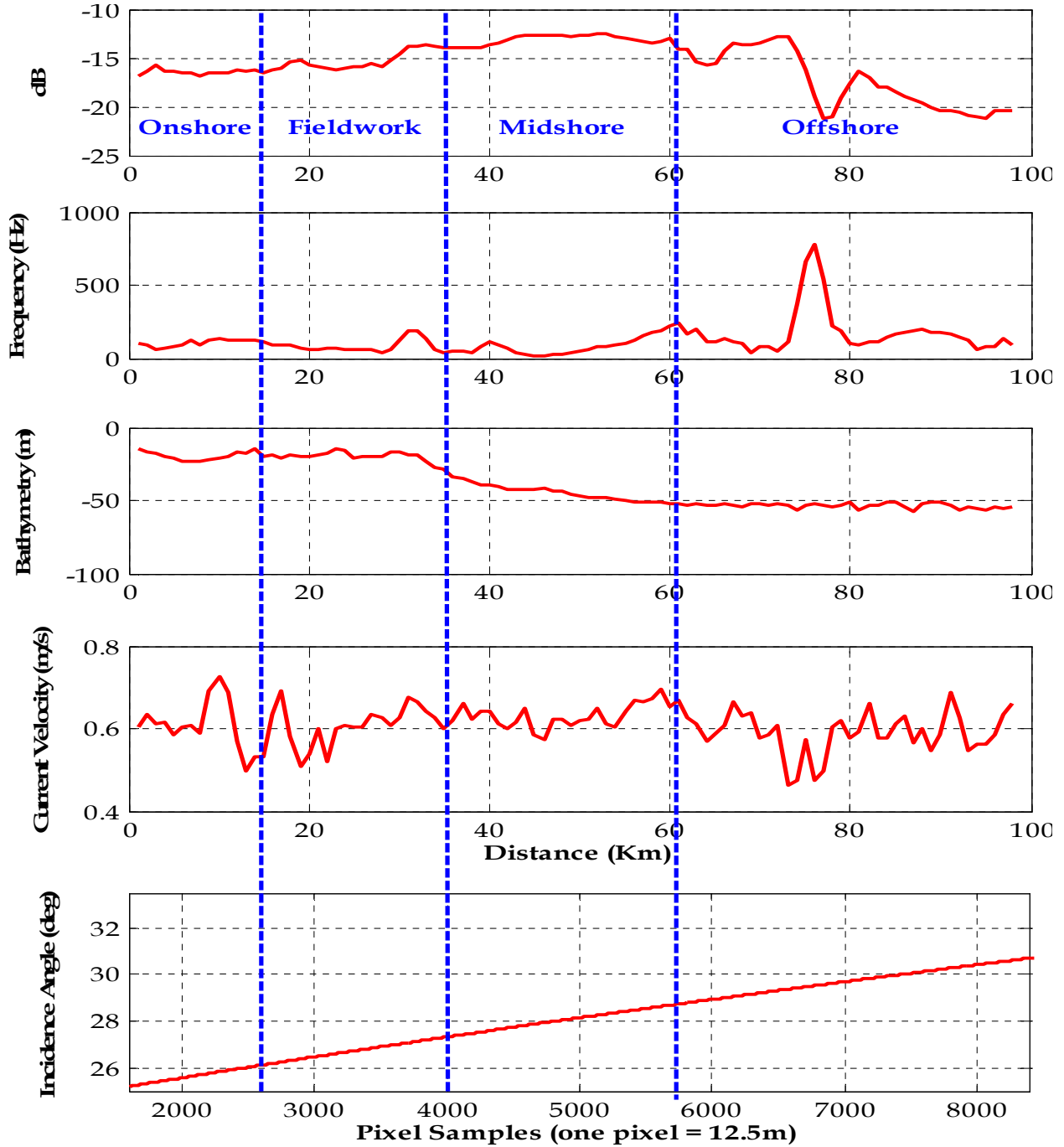
Figure 6. Comparison between physical properties of RADARSAT-1 SAR extend high-6 mode and the Bathymetry in the onshore and offshore.

confirm the studies of Wrytki (1961), Zelina et al. (2002) and Maged and Mazlan (2009) Maged et al. (2010), where, March represents the northeast monsoon wind season, in which the current flows, from northeast direction and then tends to move parallel to the coastline. Further, the current flows are deviated from the range direction which confirms the study of Maged and Mazlan (2009). Figure 8 shows significant correlations between the result of sea surface current velocities which is simulated from RADARSAT-1 SAR Wid-3, Extended High-6, and Standard-2 modes and the result extracted

from AWAC in the in-situ measurement on March 21, 25, and 31, 2005, respectively. Figure 7 illustrates how the correlation coefficient changes as the linear relationship between the two variables is altered. While in regression the emphasis is on predicting one variable from the other, in correlation the emphasis is on the degree to which a linear model may describe the relationship between two variables. Clearly, there is a good relationship between the two variables with R^2 of 0.75 for RADARSAT-1 SAR Wid-3 and AWAC on March 21, 2005 and R^2 of 0.72 for RADARSAT-1 SAR Extended High-6 and AWAC on
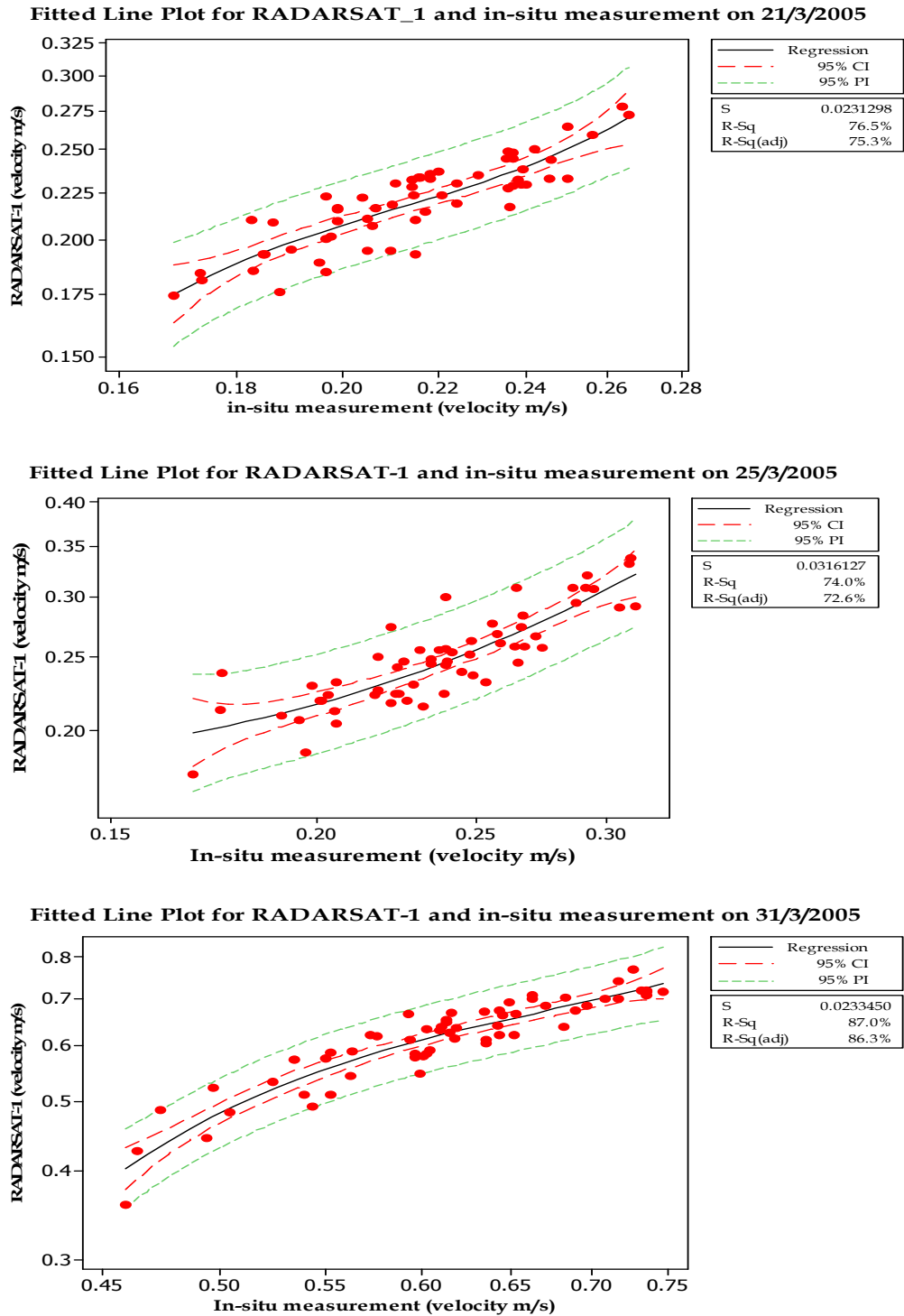
Figure 7. Comparison between physical properties of RADARSAT-1 SAR Standard-2 mode and the bathymetry along the study area.

Table 1. Average sea surface current velocities simulated from RADARSAT-1 SAR Wide-3, extended high-6, and standard-3 modes.

RADARSAT-1 SAR Image	Location		
	Onshore	Midshore	Offshore
Wide-3	0.30	0.25	0.23
Extended High-6	0.31	-----	----
Standard-2	0.73	0.68	0.50

Fitted Line Plot for RADARSAT_1 and in-situ measurement on 21/3/2005

Fitted Line Plot for RADARSAT-1 and in-situ measurement on 25/3/2005

Fitted Line Plot for RADARSAT-1 and in-situ measurement on 31/3/2005

Figure 8. Regression model between RADARSAT-1 SAR different modes simulated current and in situ measurements.

March 25, 2005. However, this relationship is not perfect, but seems to have a positive linear relationship and corresponds to what one would expect when considering two variables that are correlated and following the assumption of normality.

A scatter diagram of the correlation was used to determine the relationship between the RADARSAT-1SAR Standard-2 mode and AWAC on March 31, 2005 (Figure 8). The more surprising correlation is clear in Figure 8 with R² of 0.86. The linear relationship is good

and perfect, except for some very small outliers which exert enough influence to lower the correlation coefficient from 1 to 0.86. There was a significant positive correlation between the RADARSAT-1 SAR Standard-2 mode with *in-situ* measurement. The goodness of the regression between the two variables appears in the high positive result of regression with R^2 of 0.86. The results of the sea surface current velocities which have been extracted according to the model agree with the results of the sea surface current velocities which have been collected by AWAC in the fieldwork area. The study shows that there also can be some variations in the sea surface current velocities extracted from RADARSAT-1 with different modes and sea surface current velocities collected by AWAC in the fieldwork. These variations in current velocities depend on the image backscatter, incidence angle, and other unknown factors.

S2 mode data performed better for retrieval of sea surface current in comparison with W3 and Extended High-6 mode data. In fact, S2 mode data have a lower signal-to-noise due to their HH polarization with a wavelength of 6.6 cm and frequency of 5.3 GHz. Further, S2 mode data have 3.1 looks and steeper incidence angle of 23.7° and 31.0° than W3 and Extended High-6 mode (Maged and Mazlan, 2008; Maged et al., 2009). Thus, S2 mode data cover a swath width of 100 km and ground range resolution of 25 × 28 m. In addition, W3 is used as one of the beams to form ScanSAR Wide A (SWA) product but is not recommended for individual image because it contains a nadir ambiguity (narrow white vertical strip in the image). Since Extended High-6 mode data operate outside the optimum scan angle range of the SAR antenna, some minor degradation of image quality can be expected when compared with the Standard beam mode (RADARSAT International, 2010). The computational efficiency of sea surface current from S2 mode data, therefore, is improved and fit for real-time processing. In general, SAR Ocean current modelling which is based on Doppler centroid analyses through future research, perhaps, can provide more accurate and less ambiguous sea surface current flows in SAR data. This confirms the study of Maged and Mazlan (2008).

Conclusion

This paper has demonstrated the method to compute the sea surface current from different RADARSAT-1 SAR mode data of Wide-3, Extended High-6, and Standard-2 modes, respectively. The Doppler spectra model has been performed to simulate sea surface current. The maximum sea surface current of 0.7 m/s is observed onshore over water depth of 10 m. The regression model indicated that Doppler spectra model is an appropriate algorithm to compute the quantity information of sea surface current. In addition, RADARSAT-1 SAR Standard-2 mode showed accurate simulation of sea

surface current in comparison to Wide-3, Extended High-6 mode data with R2 of 0.86.

REFERENCES

Alpers WR, Ross DB, Rufenach CL (1981). On the detectability of ocean surface waves by real and synthetic aperture radar. J. Geophy. Res., 86: 6481-6498.

Gonzalez FI, Rufenach CL, Shuchman RA (1981). Ocean surface current detection by synthetic aperture radar. In Gower JFR. (Ed.), Proceedings of the COSPAR/SCOR/IUCRM symposium on oceanography from space (pp. 511-523). New York, NY.

Hasselman K (1980). A simple algorithm for the direct extraction of the two dimensional surface image spectrum from the return signal of synthetic aperture radar, Int. J. Remote Sens., I: 219-240.

Inglada J, Garello R (1999). Depth estimation and 3D topography reconstruction from SAR images showing underwater bottom topography signatures. In Proceedings of Geosci. Remote Sens. Symposium, 1999, IGARSS'99, Hamburg, Germany, 28 June-2 July 1999, IEEE Geoscience and Remote Sensing Society, USA. 2: 956-958.

Inglada J, Garello R (2002). On rewriting the imaging mechanism of underwater bottom topography by synthetic aperture radar as a Volterra series expansion. IEEE J. Oceanic Eng., 27: 665-674.

Maged MM (1994). Water circulation pattern of Kuala Terengganu. M.Sc. Thesis, Universiti Putra Malaysia, Kuala Lumpur, Malaysia.

Maged M, Mazlan H (2006). Three–Dimensional Reconstruction of bathymetry Using C-Band TOPSAR. Data. Photogrammetri-Fernerkundung Geoinformation. 6/2006, S. pp. 469-480.

Maged M, Mazlan H (2008). Robust Model for sea Surface Current Simulation from RADARSAT-1 SAR data. J. Convergence Inf. Technol., 3(2): 45-49.

Maged M, Hashim M, Cracknell A (2009). 3D Reconstruction of coastal bathymetry from AIRSAR/POLSAR data. Chin. J. Oceanol. Limnol., 27(1): 117-123.

Maged M, Cracknell A, Hashim M (2009). Comparison between radarsat-1 SAR different data modes for oil spill detection by a fractal box counting algorithm. Intl. J. Digital Earth, 2(3): 237-256.

Maged M, Hashim M (2009). Robust of doppler centroid for mapping sea surface current by using radar satellite data. Am. J. Eng. Appl. Sci., 2(4): 781-788.

Maged M, Arthur PC, Mazlan H (2010). 3-D visualizations of coastal bathymetry by utilization of airborne TOPSAR polarized data. International Journal of Digital Earth, 1753-8955, 3(2): 187-206.

RADARSAT International, (2010). RADARSAT applications [online]. Available from http:\www.rsi.ca [Accessed 3 September, 2010].

Rufenach CL, Shuchman RA, Lyzenga DR (1983). Interpretation of synthetic aperture radar measurements of ocean currents. J. Geophys. Res., 88: 1867-1876.

Rufenach CL, Alpers W (1981). Imaging ocean waves by synthetic aperture radars with long integration times. IEEE Trans. Antennas Propagate, AP- 29: 422-423.

Wittgenstein SL (1992). Barriers to the use of remote sensing in providing environmental information. J. Environ. Monitoring Assessment, 20(2-33) March, 1992. ISSN 1573-2959, pp. 159-166.

Wrytki K (1961). Physical oceanography of the South-East Asian Waters. In NAGA Report Vol. 2. University of California Seripps Institute of Oceanography, La Jolla, California.

Zelina ZI, Arshad A, Lee SC, Japar S, Law AT, Mustapha RAN, Maged MM (2000). East Coast of Peninsular Malaysia. Sea at The Millennium: An Environmental Evaluation. In (Ed) Charels Sheppard. Oxford.Vol II, pp. 345-359.